nature photonics

Article

https://doi.org/10.1038/s41566-023-01214-z

Interface between picosecond and nanosecond quantum light pulses

Received: 23 November 2022

Accepted: 18 April 2023

Published online: 25 May 2023

Check for updates

Filip Sośnicki ✉, Michał Mikołajczyk, Ali Golestani & Michał Karpiński ✉

Light is a key information carrier, enabling worldwide, high-speed data transmission through a telecommunication fibre network. This information-carrying capacity can be extended to transmitting quantum information (QI) by encoding it in single photons—flying qubits. However, the various QI-processing platforms operate at vastly different timescales. QI-processing units in atomic media, operating within nanosecond to microsecond timescales, and high-speed quantum communication, at picosecond timescales, cannot be linked efficiently because of the orders-of-magnitude mismatch in the timescales or, correspondingly, spectral linewidths. Here we develop a large-aperture time lens using wide-bandwidth electro-optic phase modulation to bridge this gap. We demonstrate coherent, deterministic spectral bandwidth compression of quantum light pulses by more than two orders of magnitude with high efficiency. This will facilitate large-scale hybrid QI-processing by linking the ultrafast and quasi-continuous-wave experimental platforms, which until now, to a large extent, have been developing independently.

Single photons are perfect candidates for transmitting quantum information (QI) between different quantum systems[1,2]. The timescales of such quantum light pulses can vary substantially depending on the platform employed. The single-photon pulse duration is linked to its spectral bandwidth via the time–bandwidth product, which places a lower limit on the spectral bandwidth required to support a pulse of a given duration[3]. Two classes of QI-processing platform can be distinguished based on the timescale and spectral bandwidth as criteria[4].

The first class comprises ultrafast systems, where the employed photon durations are on the order of single picoseconds, corresponding to hundreds of gigahertz of spectral bandwidth[5]. These are based mostly on optical nonlinearities such as three- or four-wave mixing, with particular examples being the widely used spontaneous parametric downconversion (SPDC) photon-pair sources and nonlinear optical gating[6,7]. Furthermore, they can be implemented with a high repetition rate. Thanks to the similar spectral bandwidths used in classical telecommunication, they are also compatible with already existing high-speed telecommunications fibre networks[8].

The second class comprises slower systems with nanosecond-long pulses and megahertz- to single gigahertz-wide spectra. It primarily includes matter-based systems, such as single atoms[9,10] or their ensembles[11–13]. It also incorporates colour centres in diamond[14], solid-state QI-processing platforms[15,16] and optomechanics[17]. Such systems provide quantum memories with long storage times[18–20] and the single-photon nonlinearities[21,22] required to perform optical QI processing, but they are inherently slow. For example, a system with 10-MHz spectral bandwidth is fundamentally limited to operate with a repetition period of at most 100 ns.

Large-scale QI processing is envisioned to take the advantages of systems from both classes, creating a hybrid quantum network or a quantum Internet[23,24]. One challenge involves efficiently connecting the two classes of quantum systems to combine the QI-processing capabilities of the slow systems with the photon-generation and efficient communication capabilities, as well as speed, of the fast systems.

One possible solution is staying within the slow regime, employing mostly matter-based platforms[25,26]. One could use known methods to generate spectrally narrow, temporally long photons[16,27]. However, narrow spectra and long photon pulses limit the overall QI-processing network performance due to the low achievable repetition rates. In particular, such megahertz-wide optical pulse spectra do

Faculty of Physics, University of Warsaw, Warszawa, Poland. ✉e-mail: filip.sosnicki@fuw.edu.pl; mkarp@fuw.edu.pl

https://doi.org/10.1038/s41566-023-01214-z

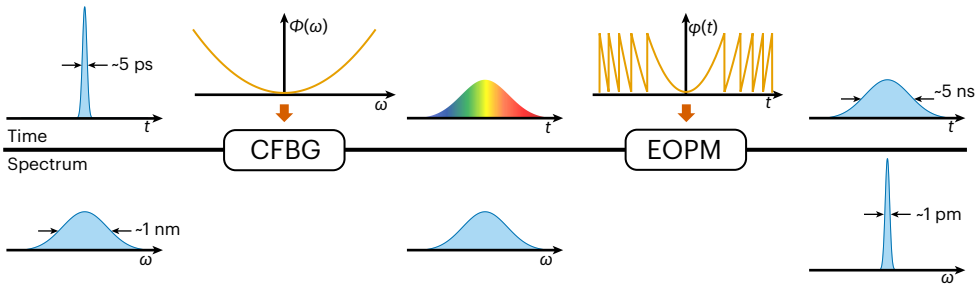

Fig. 1 | Conceptual scheme of large-scale spectral bandwidth conversion. The optical pulse's temporal profile manipulation (top) and its spectral manipulation (bottom). It begins with a Fourier-limited, ultrafast optical pulse, which is chirped in a highly dispersive chirped fibre Bragg grating (CFBG), increasing its duration from single picoseconds to single nanoseconds. This chirp linearly separates different spectral components of the optical pulse in time due to an applied quadratic spectral phase $\phi(\omega)$. Time-dependent spectral shear is then applied in the form of a quadratic modulo 2π temporal phase via electro-optic phase modulator (EOPM), shifting all the spectral components towards the central wavelength, hence performing spectral compression. By using a phase periodicity of 2π, nanosecond-long temporal waveforms are achieved, resulting in compression of the spectral width of optical pulses by many orders of magnitude, to sub-gigahertz widths.

not take advantage of the entirety of the available optical bandwidth of wavelength-division multiplexing (WDM).

A different approach relies on directly connecting ultrafast and matter-based systems. However, this results in spectral filtering of broadband photons[28], which is inherently lossy, again reducing the network performance. For example, reducing the single-photon bandwidth by a factor of N is probabilistic with a success rate of approximately $1/N$. This probability scales exponentially as $(1/N)^M$ with the number M of such interfaces.

A coherent interface, enabling low-loss shaping of quantum light pulses in time and spectrum, is thus required to efficiently combine the two classes of quantum devices to form a quantum network operating at a high repetition rate[29,30]. Such an interface needs to redistribute the energy across the single-photon pulse, simultaneously increasing its duration and narrowing its spectrum. It needs to be realized using phase-only operations, without resorting to filtering or amplification, and with low insertion loss. It requires a combination of pulse propagation in a dispersive medium combined with time-dependent phase modulation.

The quantum interfaces based on phase-only operations demonstrated so far allow for spectral manipulations only within the ultrafast regime, that is, from multi-terahertz down to tens-of-gigahertz spectral widths[31], or only within the slow regime[32,33]. Previous works have reported spectral bandwidth conversion obtained either by optical three-wave mixing[29,34] or cross-phase modulation[35]. Single-photon-level light manipulation using the four-wave-mixing scheme has also been demonstrated[36,37]. However, the nonlinear approaches suffer from high insertion losses and optical noise due to the limited conversion efficiency and the use of a strong pump. The electro-optic approach was the first to demonstrate efficient coherent spectral bandwidth modification of single-photon[30,38] or photon-pair pulses[39], thanks to its deterministic nature. It has inherent unit conversion efficiency with a limiting factor of only technical losses and allows for easy central wavelength tunability. Additionally, spectral-temporal manipulation of single-photon pulses employing electro-optic phase modulation can be performed in a low-loss, all-fibre platform without the need for optical pumping, thus without adding optical noise to the quantum signal[30]. However, until now, high spectral modification factors, necessary for linking the ultrafast and slow QI-processing platforms, have not been realized electro-optically due to the limited electro-optic phase-modulation amplitude[40,41].

In this Article we present a quantum interface based on phase-only operations, bridging the ultrafast and slow classes of QI-processing systems. We overcome the limit of electro-optic modulation amplitude by exploiting the phase periodicity, in analogy to a Fresnel lens[42]. We replace a standard parabolic electro-optic waveform with a phase-wrapped one. By combining it with off-the-shelf low-loss dispersive elements and advanced wide-bandwidth electronics, we demonstrate a quantum interface able to efficiently compress the single-photon spectral bandwidth by orders of magnitude, from picosecond to nanosecond timescales[43].

Spectral bandwidth compression requires the manipulation of both the temporal envelope and the spectrum of an optical pulse. It consists of two stages (Fig. 1). First, a spectrally wideband optical pulse is chirped in a dispersive medium. It increases the duration of the pulse, while simultaneously linearly separating its different spectral components in time. Chirping corresponds to the application of a quadratic spectral phase $\phi(\omega) = \Phi\omega^2/2$, where Φ is the group delay dispersion (GDD) and ω is the angular frequency. Subsequently, a time-dependent spectral shear is applied to the pulse such that all spectral components are shifted towards a single central wavelength, reshaping the spectrum into a narrower one. This is achieved by applying a quadratic temporal phase $\varphi(t) = Kt^2/2$, where K is the chirping factor and t is the retarded time. It can also be viewed as a spectral shift changing linearly in time[44]. When the condition $K = \Phi^{-1}$ is met, different spectral components are shifted directly towards the centre of the pulse spectrum. One obtains this by modulating the optical pulses via electro-optic phase modulation driven by a voltage signal quadratic in time. Such an operation is called a time lens due to its mathematical analogy to a quadratic spatial phase introduced by a regular lens[40,41].

Chirping single-picosecond pulses to a nanosecond duration requires a highly dispersive medium with the lowest possible loss. For this reason, we use chirped fibre Bragg gratings (CFBGs) with dispersion of 5 or 10 ns nm^{-1}, commercially available at telecommunication wavelengths with insertion losses below 3 dB.

The duration of the quadratic temporal phase has to match the output nanosecond duration of the optical pulse. The standard approach of using a single-tone radiofrequency (RF; sine) signal driving an electro-optic phase modulator (EOPM) limits the achievable compression factor. This is because of the low modulation frequency, required to cover the whole nanosecond-long output optical pulse. Combined with the limit on the maximal phase-modulation amplitude, due to the breakdown voltage of the electro-optic modulator, this limits the achievable spectral shifts, yielding a low compression factor[30,38,40,41]. Here we tackle this challenge by using a modulation scheme with an arbitrary temporal phase, taking advantage of the phase periodicity[43], that is, using a quadratic temporal phase modulo 2π factor. Such an approach, inspired by the spatial Fresnel lens[42], allows us to achieve a very long parabolic phase with steep slopes while limiting the necessary

https://doi.org/10.1038/s41566-023-01214-z

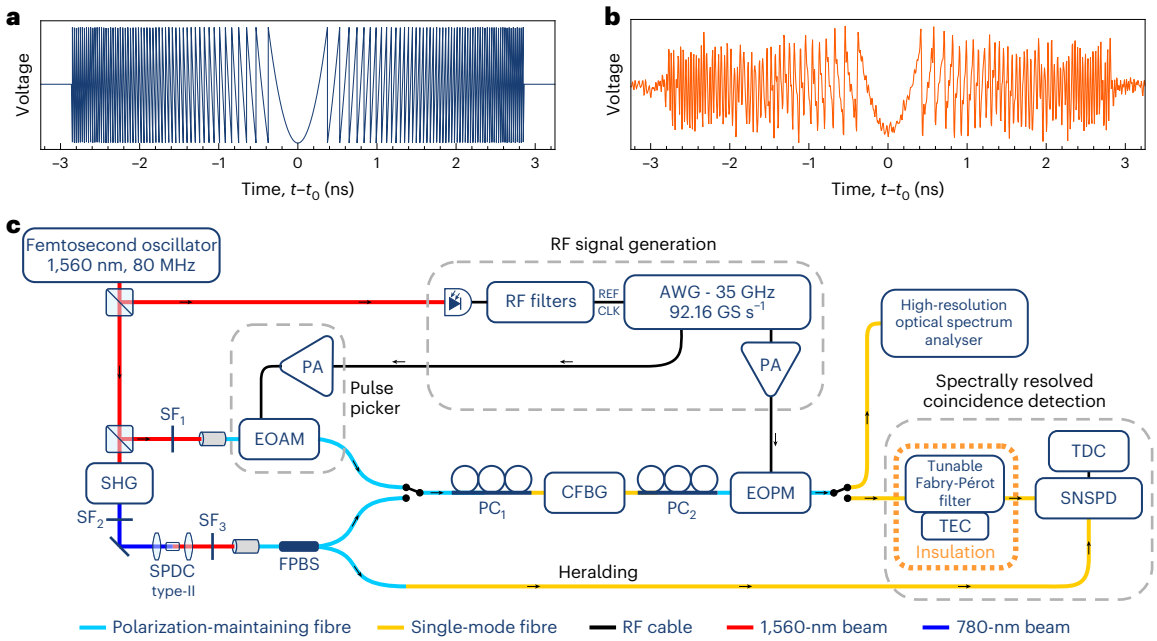

Fig. 2 | Experimental set-up and Fresnel waveforms. a, The analytical form of the Fresnel waveform, $V(t) = t^2 \mathrm{mod} 2\pi$. **b**, A measured oscilloscope (63-GHz electronic bandwidth) trace of the generated Fresnel waveform, corresponding to dispersion of 10 ns nm^{-1}. This was precompensated (Methods), transmitted through the entire RF system, and measured at the RF output of the EOPM. **c**, Schematic of the experimental set-up. The optical pulses originating in an Er-doped femtosecond oscillator and amplifier are divided into three paths by a set of beamsplitters. In the first, they are directly detected via a photodiode followed by a set of RF filters to generate a clock signal for RF system synchronization. In the second path, optical pulses are spectrally shaped (SF$_1$) and passed through a home-built pulse-picker using an electro-optic amplitude modulator (EOAM) to decrease the repetition rate. They are then chirped in a CFBG placed between two polarization controllers (PC$_{1,2}$), spectrally compressed in an EOPM driven by an amplified (PA) RF signal from an AWG and measured by a high-resolution optical spectrum analyser. Single-photon measurements utilize the third path, where optical pulses are frequency-doubled (via second harmonic generation, SHG) to generate photon pairs in a type-II SPDC process. The photon pairs are split in a fibre polarization beamsplitter (FPBS), where one of them—the herald—is sent directly to a superconducting nanowire single-photon detector (SNSPD) and time-tagged (in a time-to-digital converter, TDC) for coincidence counting. The signal photon undergoes the same spectral compression as the classical optical pulses, but is detected by another SNSPD after passing through a high-finesse Fabry–Pérot filter stabilized by a thermoelectric cooler (TEC). The filter is swept by a piezo element driven by a programmable power supply to retrieve information on the single-photon spectra. Additionally, the filter emulates a narrowband absorber, such as an atomic system.

modulation amplitude to just 2π, which is accessible for commercially available EOPMs. We note that related techniques have been used to generate ultrashort optical pulses from a continuous-wave (c.w.) laser[45,46], but without focusing on the efficiency, which is crucial for quantum applications.

The generation of Fresnel-like waveforms requires using advanced wide-bandwidth, RF electronics. In particular, one needs a high-speed arbitrary waveform generator due to the waveform complexity. In contrast to the standard electro-optic time lens, where a single-frequency signal is used, a Fresnel waveform contains a wide range of frequencies, with the highest frequency components originating from the wrapping points (Fig. 2a). Additionally, the instantaneous frequency of a quadratic function—its slope—increases linearly in both directions from the waveform's centre, with its maximal value limited by the RF system's electronic bandwidth, f_{BW}. This induces a limitation on the waveform duration and on the maximal achievable spectral shift at the edges of the waveform[44]. As a consequence, it restricts the maximal spectral width of the input optical pulses to $\Delta f = 2f_{BW}$. Our selection of RF equipment with ~35-GHz RF bandwidth limits the maximal spectral shift to 35 GHz, which yields a 0.56-nm-wide (70 GHz) spectral input window at telecom wavelengths. The non-flat frequency responses of all the RF electronics introduce distortions of the generated waveform, which contribute to the aberrations of the time lens. We used frequency-response precompensation (Methods) to counteract these. An example oscilloscope (63-GHz electronic bandwidth) trace is shown in Fig. 2b, measured at the output of the whole RF system, shown in Fig. 2c.

First, we directly show the spectral compression by employing classical light pulses, using the set-up shown schematically in Fig. 2c. The optical pulses from the erbium-doped fibre oscillator and amplifier were spectrally filtered (SF$_1$), pulse-picked and then chirped in a CFBG module. A temporal phase in the form of a Fresnel waveform was then applied in the EOPM. Finally, the laser pulses were detected with a high-resolution (5 MHz) optical spectrum analyser. The applied phase waveforms were generated with an arbitrary waveform-generator (AWG) and synchronized to the optical pulses by its internal phase-lock loop (PLL; Methods).

Figure 3a presents the input and compressed spectra when a chirping module with a dispersion of 10 ns nm^{-1} and a 20-MHz pulse repetition rate was used. The inset shows the same spectrum within a narrower wavelength range, where each point originates from an individual longitudinal mode of the laser (Methods). The spectra are normalized to the maximal intensity of the input spectrum. Both spectra are measured at the output of the whole system, whose power transmission was 31.9%. We show 154-fold (without losses) or 49-fold (including losses) enhanced maximal intensity, with a full-width at half-maximum (FWHM) of 1.37 ± 0.05 pm (169 ± 7 MHz), measured by fitting a Gaussian profile to the compressed spectral peak. This yields an efficiency of 40%, measured as a fraction of the light intensity within the compressed peak. The non-unit value of efficiency results from the imperfections of the generated Fresnel waveform—its aberrations, which cause shifting of some spectral components in the wrong direction. This effect contributes to the low spectral peaks outside the compressed window in Fig. 3a. We discuss the time-lens aberrations in more detail in Supplementary Section 3. The measured

https://doi.org/10.1038/s41566-023-01214-z

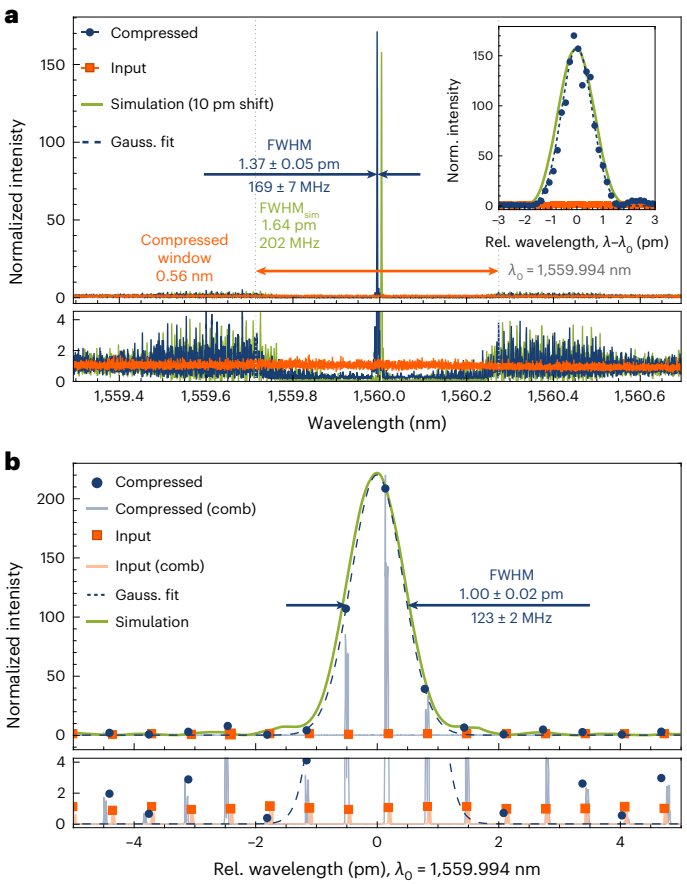

Fig. 3 | Spectral compression of coherent laser pulses. a, Spectra of input (orange), compressed (blue) and simulated (green) coherent laser pulses using a CFBG module with dispersion of 10 ns nm^{-1}, normalized to the maximum of the input spectrum. The bottom panels present the same spectra for low values of normalized intensity (also in **b**). The inset shows the same spectrum in the narrower range of 6 pm, where each point originates from an individual longitudinal mode (Methods), which samples the spectral envelope. To increase the number of measurement points, the laser light was pulse-picked to reduce the repetition rate to 20 MHz, hence increasing the density of longitudinal modes. The spectral compression factor of 408 and maximal spectral intensity enhancement by a factor of 154 results in a compression efficiency of 40% (ref. 43). The plot does not include the 31.9% transmission of the set-up due to technical losses. **b**, Increasing the dispersion to 15 ns nm^{-1} yields even higher enhancement of the maximal intensity. Here we have disabled the pulse-picking, resulting in the generation of quasi-c.w. light, with the output pulse duration approaching the pulse repetition period. The light blue lines show the raw measured spectrum, with distinct longitudinal modes of the optical pulses. Due to the width of the spectral envelope close to the repetition rate, which is equal to the longitudinal modes separation, only a single longitudinal mode dominates, confirming the quasi-c.w. regime.

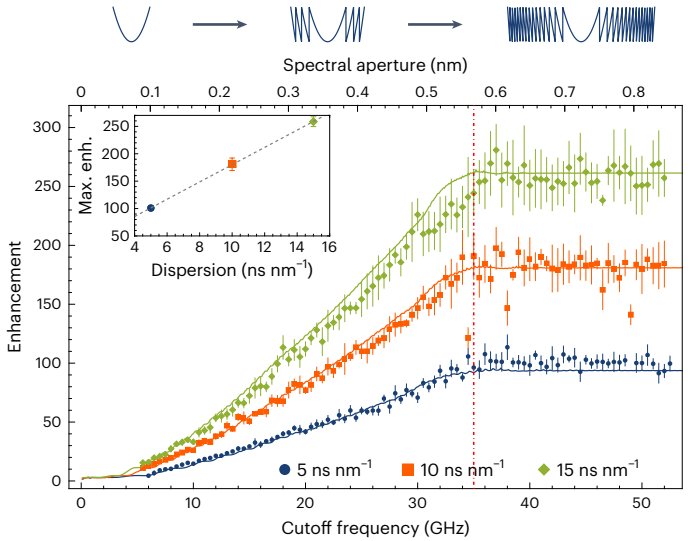

Fig. 4 | Fresnel time-lens aperture. By artificially limiting the Fresnel-waveform duration, that is, the time-lens aperture, as shown in the top panel, we measure the lossless enhancement for three different dispersions: 5 (blue), 10 (orange) and 15 ns nm^{-1} (green). The limitation is given by the maximal instantaneous frequency of the parabola, which also yields the maximal spectral shift. The enhancement increases linearly up to the RF bandwidth f_{BW}, shown with a red dot-dashed line. The presented enhancement values were determined by sweeping the RF signal amplitude (in 91 steps) while measuring the spectral compression enhancement. This dependence was fitted with a Gaussian. Its maximum yielded the reported enhancement (see Methods for more details). The error bars are based on the standard error of this Gaussian fit. Solid lines show simulation results for each value of dispersion. The inset shows the maximal enhancement as a function of the GDD, obtained as the mean enhancement for cutoff frequencies above the system RF bandwidth ± standard deviation. The dashed line in the inset is a linear fit. The output spectral bandwidths for these measurements are shown in Supplementary Fig. 1.

spectra show good agreement with simulations (Methods), shown with a green line.

Next, we increased the dispersion to 15 ns nm^{-1} by joining two CFBG modules (5 and 10 ns nm^{-1}). We also increased the repetition rate to 80 MHz by disabling the pulse-picker. By using an appropriately modified Fresnel waveform, we obtained an even higher enhancement of over 220 (without loss) and an efficiency of 38% (Fig. 3b). However, due to the use of two separate CFBG modules, introducing an increased total loss of 16%, including the EOPM, the enhancement with system transmission taken into account was 35.2. Here we also show the generation of quasi-c.w. light. The FWHM of the compressed spectra is 1.00 ± 0.02 pm (123 ± 2 MHz), which is very close to the repetition rate of 80 MHz. This means that one longitudinal mode dominates under the spectral envelope, as shown in Fig. 3b, where the blue, dashed line shows the fitted Gaussian envelope, and the raw measured spectrum, with clearly visible laser longitudinal modes (comb), is shown by the light blue line (Methods). The measured temporal profiles of the output pulses are presented in Supplementary Section 2 and Supplementary Fig. 2.

To confirm the contribution of the phase-wrapped part of the Fresnel waveform to the spectral compression, we measured the enhancement when artificially limiting the duration of the waveform. Because the instantaneous frequency of the signal, proportional to its slope, increases linearly for the quadratic function, we limited the waveform up to the point where it meets the cutoff frequency f_{max}, which we changed in the range of 5–52 GHz (Fig. 4). We show a nearly linearly increasing enhancement with the cutoff frequency up to the bandwidth of the RF system of 35 GHz, after which we reach a plateau. This clearly shows that the Fresnel-like waveforms take advantage of the entire available RF bandwidth. This experimental dataset can be further used to show the dependence of the output spectral bandwidth on the cutoff frequency, which we present in Supplementary Fig. 1 and discuss in Supplementary Section 1.

To directly verify our approach to large-scale spectral compression of quantum light pulses for applications in quantum networks, we prepared pure single photons via a heralded SPDC process[6] pumped with frequency-doubled laser pulses originating from the same laser as above (Fig. 2c and Methods). The single photons were then propagated through the same 10 ns nm^{-1} CFBG and EOPM as for the case of classical light. Finally, they were detected with a superconducting

https://doi.org/10.1038/s41566-023-01214-z

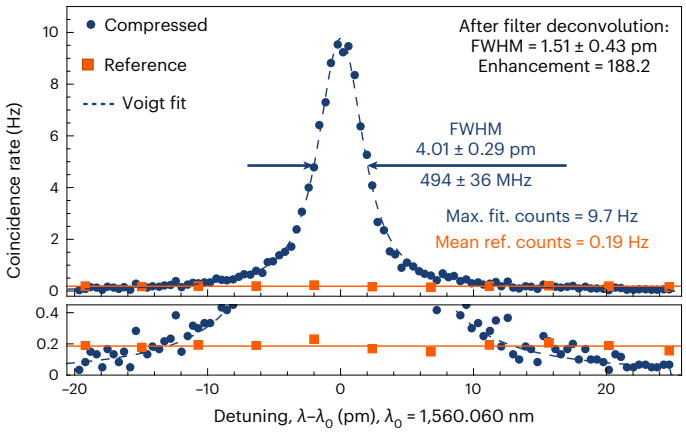

Fig. 5 | Spectral manipulation of single-photon wavepackets. Coincidence counts of heralded photons passing through a narrowband filter with compression (blue dots) and without compression (orange squares). To avoid introducing arbitrary parameters, the reference signal was measured for photons going through the same set-up, but without applying temporal phase (Methods), while the transmission of 31.9% of the set-up was measured separately. The coincidence rate was measured for 1 min per bin for the compressed signal and 5 min per bin for the reference signal. The filter was detuned to measure the spectral shape of the spectrum with the results fitted with a Voigt profile (see main text). The bottom panel presents the same data for low values of coincidence counts.

nanowire single-photon detector after passing through a high-finesse tunable Fabry–Pérot interference filter with 420-MHz FWHM spectral bandwidth (Methods), simulating a narrowband absorber like an atomic system. Then, coincidences of the signal and idler photons were found with a time-to-digital converter. In Fig. 5 we show the measured 51-fold-increased heralded single-photon flux of the compressed single-photon spectra (blue) in comparison to the input (orange) in the case of a lossless system. Taking into account the technical transmission of the CFBG and EOPM of 31.9% results in an overall enhancement of 16. This proves that such a system can be used to enhance the absorption or interference rates of bandwidth-incompatible photon pulses. The 16-fold enhancement would be further improved using a spectrally narrower absorber; here, the absorption line was larger than the single-photon spectral width, thus limiting the obtained enhancement.

To find the upper bound of the enhancement for an absorber with linewidth much smaller than the single-photon spectral width, we measured the single-photon spectral shape by detuning the Fabry–Pérot interference filter. This was then fitted with the Voigt profile, shown by the blue dashed line in Fig. 5. Such a profile is a convolution of the single-photon spectrum's Gaussian shape and the interference filter's Lorentzian shape with a fixed width measured independently. Deconvolving the Gaussian width from the fit yields a single-photon spectral width of 1.51 ± 0.43 pm (186 ± 53 MHz) and enhancement (without technical losses) of 188.2, which agrees well with the results for classical light shown in Fig. 3a. Including the 31.9% transmission of the system, we expect enhancement of the absorbed single-photon flux by a factor of up to 60 for absorber linewidths smaller than the compressed single-photon spectral width.

We have demonstrated that wideband arbitrary electro-optic temporal phase modulation enables the spectral compression of classical and quantum light pulses by over two orders of magnitude, from tens of gigahertz to hundreds of megahertz, reaching the regime of matter-based QI-processing platforms. To this end we have developed a Fresnel time lens, which takes advantage of phase periodicity and all of the available RF system bandwidth. We applied this method to reduce the spectral bandwidths of heralded single photons down to a single picometre, while enhancing maximum of their spectral intensity distribution. Additionally, delaying the RF waveform with respect to the single-photon pulses allows fine-tuning of the output spectrum central wavelength[44]. By simulating a narrowband absorber with a narrowband filter we measured a 16-fold increase of photon flux through the filter as compared to a direct connection. We expect to further increase this value to 60 for absorbers with spectral linewidths narrower than the compressed pulse spectrum. Such a low-loss, all-fibre and easily reconfigurable electro-optic quantum interface will allow us to increase the absorption and/or multi-photon interference rates in future hybrid quantum networks, where both ultrafast and atomic-based systems will be used. Not only will this enable efficient network operation, but it may facilitate the efficient establishment of long-distance entanglement between quantum network nodes.

The development of high-speed RF devices with commercially available bandwidths of 70 GHz, as well as lower-loss CFBGs will allow us to further boost the performance of such electro-optic quantum interfaces. Increasing the available RF bandwidth will, in particular, increase the Fresnel time-lens temporal aperture while reducing aberrations caused by the non-ideal phase wrappings. Moreover, our device shows high potential to be used in an on-chip configuration, where bandwidths over 100 GHz with low V_π have been reported in a thin-film lithium niobate platform[47–50]. Finally, using a phase-wrapped (Fresnel) temporal phase modulation is a substantial step towards arbitrary shaping of quantum light in the spectro-temporal degree of freedom[3,51,52].

Online content

Any methods, additional references, Nature Portfolio reporting summaries, source data, extended data, supplementary information, acknowledgements, peer review information; details of author contributions and competing interests; and statements of data and code availability are available at https://doi.org/10.1038/s41566-023-01214-z.

References

1. Gisin, N. & Thew, R. Quantum communication. *Nat. Photon.* **1**, 165–171 (2007).
2. Simon, C. Towards a global quantum network. *Nat. Photon.* **11**, 678–680 (2017).
3. Karpiński, M., Davis, A. O. C., Sośnicki, F., Thiel, V. & Smith, B. J. Control and measurement of quantum light pulses for quantum information science and technology. *Adv. Quantum Technol.* **4**, 2000150 (2021).
4. Awschalom, D. et al. Development of quantum interconnects (QuICs) for next-generation information technologies. *PRX Quantum* **2**, 017002 (2021).
5. Weiner, A. M. Ultrafast optical pulse shaping: a tutorial review. *Opt. Commun.* **284**, 3669–3692 (2011).
6. Mosley, P. J. et al. Heralded generation of ultrafast single photons in pure quantum states. *Phys. Rev. Lett.* **100**, 133601 (2008).
7. MacLean, J.-P. W., Donohue, J. M. & Resch, K. J. Direct characterization of ultrafast energy-time entangled photon pairs. *Phys. Rev. Lett.* **120**, 053601 (2018).
8. Essiambre, R.-J., Kramer, G., Winzer, P. J., Foschini, G. J. & Goebel, B. Capacity limits of optical fiber networks. *J. Light. Technol.* **28**, 662–701 (2010).
9. Saffman, M., Walker, T. G. & Mølmer, K. Quantum information with Rydberg atoms. *Rev. Mod. Phys.* **82**, 2313–2363 (2010).
10. Reiserer, A., Kalb, N., Rempe, G. & Ritter, S. A quantum gate between a flying optical photon and a single trapped atom. *Nature* **508**, 237–240 (2014).
11. Lvovsky, A. I., Sanders, B. C. & Tittel, W. Optical quantum memory. *Nat. Photon.* **3**, 706–714 (2009).
12. Jensen, K. et al. Quantum memory for entangled continuous-variable states. *Nat. Phys.* **7**, 13–16 (2011).

13. Blatt, R. & Roos, C. F. Quantum simulations with trapped ions. *Nat. Phys.* **8**, 277–284 (2012).
14. Doherty, M. W. et al. The nitrogen-vacancy colour centre in diamond. *Phys. Rep.* **528**, 1–45 (2013).
15. Aharonovich, I., Englund, D. & Toth, M. Solid-state single-photons emitters. *Nat. Photon.* **10**, 631–641 (2016).
16. Lago-Rivera, D., Grandi, S., Rakonjac, J. V., Seri, A. & de Riedmatten, H. Telecom-heralded entanglement between multimode solid-state quantum memories. *Nature* **594**, 37–40 (2021).
17. Wallucks, A., Marinković, I., Hensen, B., Stockill, R. & Gröblacher, S. A quantum memory at telecom wavelengths. *Nat. Phys.* **16**, 772–777 (2020).
18. Duan, L. M., Lukin, M. D., Cirac, J. I. & Zoller, P. Long-distance quantum communication with atomic ensembles and linear optics. *Nature* **414**, 413–418 (2001).
19. Wang, Y. et al. Single-qubit quantum memory exceeding ten-minute coherence-time. *Nat. Photon.* **11**, 646–650 (2017).
20. Kaczmarek, K. T. et al. High-speed noise-free optical quantum memory. *Phys. Rev. A* **97**, 042316 (2018).
21. Fushman, I. et al. Controlled phase shifts with a single quantum dot. *Science* **320**, 769–772 (2008).
22. Tiarks, D., Schmidt, S., Rempe, G. & Dür, S. Optical π phase shift created with single-photon pulse. *Sci. Adv.* **2**, e160003 (2016).
23. Kimble, H. J. The quantum internet. *Nature* **453**, 1023–1030 (2008).
24. Wehner, S., Elkouss, D. & Hanson, R. Quantum internet: a vision for the road ahead. *Science* **362**, eaam9288 (2018).
25. Reiserer, A., Kalb, N., Rempe, G. & Ritter, S. A quantum gate between a flying optical photon and a single trapped atom. *Nature* **508**, 237–240 (2014).
26. Cacciapuoti, A. S., Caleffi, M., Van Meter, R. & Hanzo, L. When entanglement meets classical communications: quantum teleportation for the quantum internet. *IEEE Trans. Commun.* **68**, 3808–3833 (2001).
27. Ou, Z. Y. & Lu, Y. J. Cavity enhanced spontaneous parametric down-conversion for the prolongation of correlation time between conjugate photons. *Phys. Rev. Lett.* **83**, 2556–2559 (1999).
28. Michelberger, P. S. et al. Interfacing GHz-bandwidth heralded single photons with a warm vapour Raman memory. *New J. Phys.* **17**, 043006 (2015).
29. Lavoie, J., Donohue, J. M., Wright, L. G., Fedrizzi, A. & Resch, K. J. Spectral compression of single photons. *Nat. Photon.* **7**, 363–366 (2013).
30. Karpiński, M., Jachura, M., Wright, L. J. & Smith, B. J. Bandwidth manipulation of quantum light by an electro-optic time lens. *Nat. Photon.* **11**, 53–57 (2017).
31. Allgaier, M. et al. Highly efficient frequency conversion with bandwidth compression of quantum light. *Nat. Commun.* **8**, 14288 (2017).
32. Specht, H. P. et al. Phase shaping of single-photon wave packets. *Nat. Photon.* **3**, 469–472 (2016).
33. Mazelanik, M., Leszczyński, A., Lipka, M., Parniak, M. & Wasilewski, W. Temporal imaging for ultra-narrowband few-photon states of light. *Optica* **7**, 203–208 (2020).
34. Agha, I., Ates, S., Sapienza, L. & Srinivasan, K. Spectral broadening and shaping of nanosecond pulses: toward shaping of single photons from quantum emitters. *Opt. Lett.* **39**, 5677–5680 (2014).
35. Matsuda, N. Deterministic reshaping of single-photon spectra using cross-phase modulation. *Sci. Adv.* **2**, e1501223 (2016).
36. Salem, R. et al. Optical time lens based on four-wave mixing on a silicon chip. *Opt. Lett.* **33**, 1047–1049 (2008).
37. Joshi, C. et al. Picosecond-resolution single-photon time lens for temporal mode quantum processing. *Optica* **9**, 364–373 (2022).
38. Sośnicki, F., Mikołajczyk, M., Golestani, A. & Karpiński, M. Aperiodic electro-optic time lens for spectral manipulation of single-photon pulses. *Appl. Phys. Lett.* **116**, 234003 (2020).
39. Mittal, S. et al. Temporal and spectral manipulations of correlated photons using a time lens. *Phys. Rev. A* **96**, 043807 (2017).
40. Kolner, B. H. Space-time duality and the theory of temporal imaging. *IEEE J. Quantum Electron.* **30**, 1951–1963 (1994).
41. Torres-Company, V., Lancis, J. & Andrés, P. Space-time analogies in optics. *Prog. Opt.* **56**, 1–80 (2011).
42. Fresnel, A. *Mémoire sur un Nouveau Système d'Éclairage des Phares* (Imprimerie Royale, 1822).
43. Sośnicki, F. & Karpiński, M. Large-scale spectral bandwidth compression by complex electro-optic temporal phase modulation. *Opt. Express* **26**, 31307–31316 (2018).
44. Wright, L. J., Karpiński, M., Söller, C. & Smith, B. J. Spectral shearing of quantum light pulses by electro-optic phase modulation. *Phys. Rev. Lett.* **118**, 023601 (2017).
45. Li, B., Lou, S. & Azaña, J. Novel temporal zone plate designs with improved energy efficiency and noise performance. *J. Light. Technol.* **32**, 4803–4809 (2014).
46. Fernández-Pousa, C. R., Maram, R. & Azaña, J. CW-to-pulse conversion using temporal Talbot array illuminators. *Opt. Lett.* **42**, 2427–2430 (2017).
47. Wang, C. et al. Integrated lithium niobate electro-optic modulators operating at CMOS-compatible voltages. *Nature* **562**, 101–104 (2018).
48. Jin, M., Chen, J., Sua, Y., Kumar, P. & Huang, Y. Efficient electro-optical modulation on thin-film lithium niobate. *Opt. Lett.* **46**, 1884–1887 (2021).
49. Zhu, D. et al. Spectral control of nonclassical light pulses using an integrated thin-film lithium niobate modulator. *Light Sci. Appl.* **11**, 327 (2022).
50. Yu, M. et al. Integrated femtosecond pulse generator on thin-film lithium niobate. *Nature* **612**, 252–258 (2022).
51. Kielpinski, D., Corney, J. F. & Wiseman, H. M. Quantum optical waveform conversion. *Phys. Rev. Lett.* **106**, 130501 (2011).
52. Ashby, J. et al. Temporal mode transformations by sequential time and frequency phase modulation for applications in quantum information science. *Opt. Express* **28**, 38376–38389 (2020).

Publisher's note Springer Nature remains neutral with regard to jurisdictional claims in published maps and institutional affiliations.

Springer Nature or its licensor (e.g. a society or other partner) holds exclusive rights to this article under a publishing agreement with the author(s) or other rightsholder(s); author self-archiving of the accepted manuscript version of this article is solely governed by the terms of such publishing agreement and applicable law.

© The Author(s), under exclusive licence to Springer Nature Limited 2023

Methods

RF waveforms generation

The waveforms were calculated with the following parameters: chirping rate of the time lens K, spectral aperture Δf (main text) and a sampling rate (SR) of the AWG of 92.16 GS s^{-1}. The duration of the entire waveform was limited to $\Delta t = 2\pi\Delta f/K$. The waveforms were then divided by the complex frequency response of the RF system (measured separately) in the frequency domain within the range of the RF bandwidth of the system. The resulting waveform in the time domain was generated in the AWG (Keysight M8196A, 35-GHz RF bandwidth), amplified with a high-bandwidth power amplifier (RFLambda, 0.2–35 GHz, 2 W). This drove an electro-optic phase modulator (EOSpace, $V_{\pi@1GHz} = 3$ V, 2.4-dB insertion loss). Every change in the waveform parameters changed its minimal and maximal values. Therefore, for each new waveform, it was necessary to find the peak-to-peak amplitude of the RF waveform that provided the peak-to-peak phase modulation depth of 2π. This was carried out by sweeping the RF amplitude while measuring the spectral compression enhancement. The dependence was fitted with a Gaussian, the centre of which provided the RF amplitude for the 2π phase modulation depth, and its maximum yielded the corresponding enhancement. The error bars in Fig. 4 were based on the standard error of this Gaussian fit.

Classical spectrum measurements

The spectra of classical, coherent light were acquired with a high-resolution optical spectrum analyser (APEX Technologies AP2681A, 5-MHz resolution). As this resolution is higher than the repetition rate of 80 MHz or 20 MHz, individual longitudinal modes were found and summed, creating a spectral envelope sampled with a resolution given by the repetition rate. The home-built pulse-picker was used to reduce the repetition rate and hence increase the resolution of the measured spectra. The pulse-picker was built by utilizing a second channel of the AWG, generating rectangular pulses, which were amplified (Keysight N4985A-S50) and used to drive an electro-optic amplitude modulator (Thorlabs LN05S-FC).

Source of heralded single photons

Laser pulses originating from an erbium-doped fibre oscillator (Menlo C-Fiber 780HP) with a repetition rate of 80 MHz and central wavelength of 1,560 nm were frequency-doubled (Menlo C-Fiber 780HP), yielding a second harmonic beam with a central wavelength of 780 nm. This pump beam passed through a 4f tunable spectral filter and was then focused into a 10-mm-long periodically poled potassium titanyl phosphate (PPKTP) crystal, where type-II SPDC took place, creating orthogonally polarized photon pairs. The pump beam was spectrally filtered to produce photon pairs that were wavelength-degenerate and spectrally uncorrelated. The photon-pair beam was recollimated and spectrally filtered with a set of interference filters to 1-nm FWHM such that the whole spectrum could be measured by sweeping the Fabry–Pérot interference filter with a free spectral range of 1.2 nm. The photon pairs were then coupled into a polarization-maintaining fibre and photons from each pair—signal and herald (idler)—were separated by a fibre polarization beamsplitter. The heralding (idler) photon was sent directly to a superconducting nanowire single-photon detector (Single Quantum) heralding the signal photon. A time-to-digital converter (Swabian Instruments TimeTagger Ultra) was used to register coincidence events of detecting heralding idler photons and heralded signal photons.

Spectrally narrowband absorber

The narrowband absorber was realized with a fibre-pigtailed high-finesse tunable Fabry–Pérot interference filter (Micron Optics FFP-TF2) with 420-MHz FWHM passband and 1.2-nm measured free spectral range. The tuning of the filter was automated with a stable programmable power supply (Keysight E36313A) driving a piezo element within the filter. Thermal isolation and precise temperature control allowed us to reduce thermal drifts to below 1 pm within the measurement time. Because of a very low count rate through the filter, due to its narrowband transmission, that is, filtering most of the photons, the coincidence count rates shown in Fig. 5 were measured without disconnecting the CFBG and EOPM. This was done to avoid introducing any arbitrary parameters such as additional polarization mismatch from fibre reconnections or thermal drift, which could not be realigned due to the low count rate. The transmission of the set-up was thus measured separately.

Simulations

The simulations were based on ref. 43. Their inputs were waveforms sent to the AWG and the measured input (reference) spectrum. The waveform was discretized in time according to the sample rate and in amplitude according to the effective number of bits of the AWG. Then, a set of complex frequency responses of the elements was applied by multiplication. By a series of applied temporal or spectral phases and fast Fourier transforms, a quadratic spectral phase and the simulated temporal phase waveform were applied to the input spectra, yielding output spectra, shown as a green line in Fig. 3, and their enhancement (solid lines in Fig. 4). The simulations do not take into account time-interval error (jitter).

Data availability

The data that support the findings of this study are available from the corresponding author on reasonable request.

Acknowledgements

We thank A. O. C. Davis, M. Jachura, C. Radzewicz, B. J. Smith, N. Treps and A. Widomski for insightful comments and discussions. We thank Keysight and AM Technologies for equipment loans. This work was funded in part by the First TEAM (project no. POIR.04.04.00-00-5E00/18; M.K., F.S. and M.M.) and HOMING (project no. POIR.04.04.00-00-1E2B/16; M.K. and A.G.) programmes of the Foundation for Polish Science, co-financed by the European Union under the European Regional Development, and in part by the National Science Centre of Poland QuantERA project QuICHE (project no. 2019/32/Z/ST2/00018; M.K. and A.G.) and Preludium (project no. 2019/35/N/ST2/04434; F.S.).

Author contributions

M.K. conceived and supervised the project. F.S. designed and performed the experiment with a contribution from M.M., who built the photon-pair source and the tunable spectral filter. A.G. contributed to the early stages of the experiment. F.S. and M.K. wrote the manuscript with input from all the authors. F.S. prepared the figures.

Competing interests

The authors declare no competing interests.

Additional information

Supplementary information The online version contains supplementary material available at https://doi.org/10.1038/s41566-023-01214-z.

Correspondence and requests for materials should be addressed to Filip Sośnicki or Michał Karpiński.

Peer review information *Nature Photonics* thanks Sunil Mittal and John Donohue for their contribution to the peer review of this work.

Reprints and permissions information is available at www.nature.com/reprints.